ISSN 1063-7745, Crystallography Reports, 2023, Vol. 68, No. 5, pp. 788–796. © Pleiades Publishing, Inc., 2023.
Russian Text © The Author(s), 2023, published in Kristallografiya, 2023, Vol. 68, No. 5, pp. 799–808.

PHYSICAL PROPERTIES OF CRYSTALS

Dedicated to the memory of L.A. Shuvalov

Calculation of the Phonon Spectrum of $PbMnBO_4$ Crystal Using Density Functional Theory

S. N. Krylova[a,*]

[a] *Kirensky Institute of Physics, Krasnoyarsk Scientific Center, Siberian Branch, Russian Academy of Sciences, Krasnoyarsk, 660036 Russia*

**e-mail: slanky@iph.krasn.ru*

Received December 27, 2022; revised January 18, 2023; accepted February 8, 2023

Abstract—The phonon dispersion and Raman spectrum of the $PbMnBO_4$ ferromagnetic crystal have been calculated within the density functional theory. Imaginary phonon branches have been observed at the points Y, Z, and Γ and along the X–S direction of the Brillouin zone, which indicates structural instability and a possible phase transition with variation in external factors (temperature and pressure). The shapes of vibrations and symmetry types of the normal modes of the crystal at the center of the Brillouin zone have been determined. The calculation results are compared with the experimental and theoretical spectra from other studies. It is shown that the vibrational mode of highest intensity at 692.5 cm^{-1} in the spectrum and the mode at 272.3 cm^{-1}, corresponding to the experimental modes at 690.5 and 224.7 cm^{-1}, are bending vibrations of oxygen atoms in distorted MnO_6 octahedra.

DOI: 10.1134/S1063774523600436

INTRODUCTION

The $PbMnBO_4$ crystal belongs to the $PbMBO_4$ orthoborate family (M = Ga, Al, Fe, Cr, Mn) [1–3], which has attracted the attention of researchers over the past two decades. The $PbGaBO_4$ compound exhibits photocatalytic properties [4–6]. Various physical properties of the $PbFeBO_4$ crystal have been studied [3, 7–12], the most interesting of which is antiferromagnetism. The $PbCrBO_4$ crystal is also an antiferromagnet [3, 7]. The orthoborate family representatives, depending on the M ion type, can be used in spintronics and photocatalysis.

The $PbMnBO_4$ crystal was first synthesized by Park's research team [3]. The magnetic properties of this material were discovered [3, 13–15]. Below the Curie temperature (T_C = 30.3 K), it is a highly anisotropic ferromagnet. Significantly strong effective magnetic anisotropy fields in the $PbMnBO_4$ crystal determine an extremely wide (for ferromagnets) energy gap in the ferromagnetic resonance spectrum of the crystal (112 GHz at T = 4.2 K) [14]. When the crystal is heated in zero magnetic field, a noticeable magnetic contribution to its specific heat is maintained up to a temperature of 60 K, twice as high as the Curie temperature T_C. These facts were explained by the chain magnetic structure of the $PbMnBO_4$ crystal [14]. Along with the magnetic properties, the dielectric properties of $PbMnBO_4$ crystal were investigated in [13], and the Raman spectra in the temperature range from 4 to 300 K, with a magnetic field applied, were measured in [16].

The unique properties of $PbMnBO_4$ crystal are caused by the specific features of its structure. The main fragments of the crystal structure are linear chains of distorted edge-sharing MnO_6 octahedra (Fig. 1). According to the crystal structure, magnetic Mn ions are ordered along the chains. The static Jahn–Teller effect causes both strong magnetic anisotropy and formation of ferromagnetic exchange coupling in chains of MnO_6 octahedra [14].

Simultaneously with the experimental examination of the crystal, a series of theoretical studies was carried out. In particular, the $PbMnBO_4$ magnetic properties were investigated using the electron density functional theory (DFT) [7]. The calculated field dependences of the magnetization and susceptibility of a classical two-sublattice ferromagnet were associated with the results of the magnetic measurements of the highly anisotropic $PbMnBO_4$ ferromagnet [17]. The phonon spectrum of this crystal at the center of the Brillouin zone was calculated [18].

The experimental temperature investigations of the Raman spectra of this crystal showed that, at low tem-

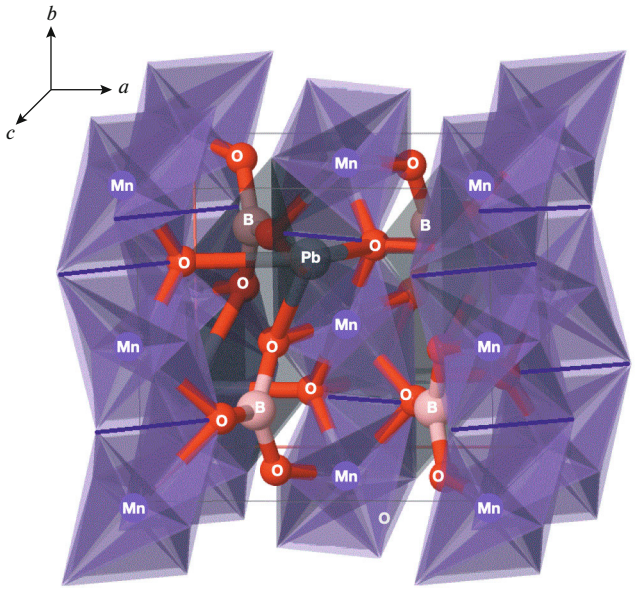

Fig. 1. $PbMnBO_4$ structure in the *Pnma* phase.

peratures, they contain soft modes [16]. This behavior of the vibrational spectrum may indicate lattice instability. The origin of these unstable modes requires a separate theoretical analysis. Therefore, this study is aimed at calculating and studying the lattice dynamics in this crystal in the *Pnma* phase. Particular attention is paid to the calculation and interpretation of the Raman spectrum of the $PbMnBO_4$ crystal.

CALCULATION PARAMETERS

The theoretical calculation was performed within the DFT plane-wave basis set using the CASTEP software package [19]. In the plane-wave basis sets, the basis functions are combinations of harmonic functions. The DFT is based on the use of electron density function instead of the wave function to describe a system. Correspondingly, the Kohn–Sham equations [20, 21] are solved instead of the Schrödinger equation.

The experimental data (lattice parameters and atomic positions) from [3] were taken as initial data. The cell geometry was optimized by minimizing the total energy using the Broyden–Fletcher–Goldfarb–Shanno algorithm [22]. A cut-off energy $E_{\text{cut-off}}$ of 910 eV was selected, and a 5 × 5 × 5 Monkhorst–Pack *k*-point mesh was applied [23]. The total energy convergence was 5.0×10^{-8} eV/atom. The norm-conserving potentials for all atoms were used. The valence electrons $2s^2$ and $2p^1$ for B, $3d^5$, $4s^2$, and $3s^2$ for Mn, $5s^2$, $5p^6$, $5d^{10}$, $6s^2$, and $6p^2$ for Pb, and $2s^2$ and $2p^4$ for O were considered. In the optimized geometry, phonon dispersion, and Raman spectrum calculations, the PBEsol (GGA) functional, most suitable for solids, was used [24, 25]. This functional includes the dependence of energy on the electron density and its gradient. As a result of the calculations, the shapes of all vibrational modes at the center of the Brillouin zone were found. The structure and vibrations were visualized in the Jmol software [26]. The spectral image was obtained using a licensed version of the Origin 2023 program [27].

PHONON DISPERSION

The lattice parameters and equilibrium positions of atoms in the unit cell were found by minimizing the forces (less than 10^{-2} eV/Å) acting on atoms with a self-consistent calculation of the total crystal energy with an accuracy of less than 10^{-6} eV. The discrepancy of the calculated energy was 1.65×10^{-7} eV per ion; the maximum force was 7.13×10^{-3} eV/Å; the maximum shift was 3.13×10^{-4} Å; and the maximum pressure was 3.01×10^{-3} GPa. The minimum in the dependence of the total crystal energy on the unit cell volume corresponds to the orthorhombic lattice parameters a = 5.86 Å, b = 6.02 Å, and c = 8.49 Å. The experimental data used as a basis in the calculation were a_{exp} = 6.70 Å, b_{exp} = 5.94 Å, and c_{exp} = 8.64 Å [2]. The calculated lattice parameter a differs from the experimental value by ~13%.

In further calculations the dispersive phonon spectrum and Raman spectrum were obtained using the calculated lattice parameters. The Brillouin zone of the orthorhombic *Pnma* phase is shown in Fig. 2. It includes the high-symmetry points Γ, *Z*, *U*, *X*, *S*, *Y*, *T*, and *R*.

Figure 3 shows the dispersion of phonons in the crystal and the phonon density of states. Three groups of branches are observed, which are separated by large gaps: ~120 cm^{-1} between the lowest-energy groups and ~210 cm^{-1} between the high-energy groups. The imaginary values of the phonon energy, which are related to the structural instability of the crystal, are indicated by negative numbers in the figure.

At the point Γ (the Brillouin zone center), there are two unstable acoustic modes B_{3u} and B_{2u} with frequencies of $0.024i$ and $0.20i$ cm^{-1}, respectively. The shapes of these unstable vibrational modes are presented in Figs. 4a and 4b. The shift of all atoms in one direction is characteristic of acoustic modes (Figs. 4a–4c).

At point *Z*, four unstable vibrations are observed (Fig. 2). Two of these four modes remain weakly unstable at the transition to the point Γ, the third is a stable B_{1u} acoustic mode (Fig. 4c), and the fourth falls into the region above zero with the A_u symmetry and a frequency of 54 cm^{-1}. This mode corresponds to the vibrations of lead and oxygen atoms (Fig. 4d). Manganese and boron atoms are not involved in this vibrational mode.

The next unstable points in the phonon branches are observed between the points *X* and *S* (line *D* in Fig. 2).

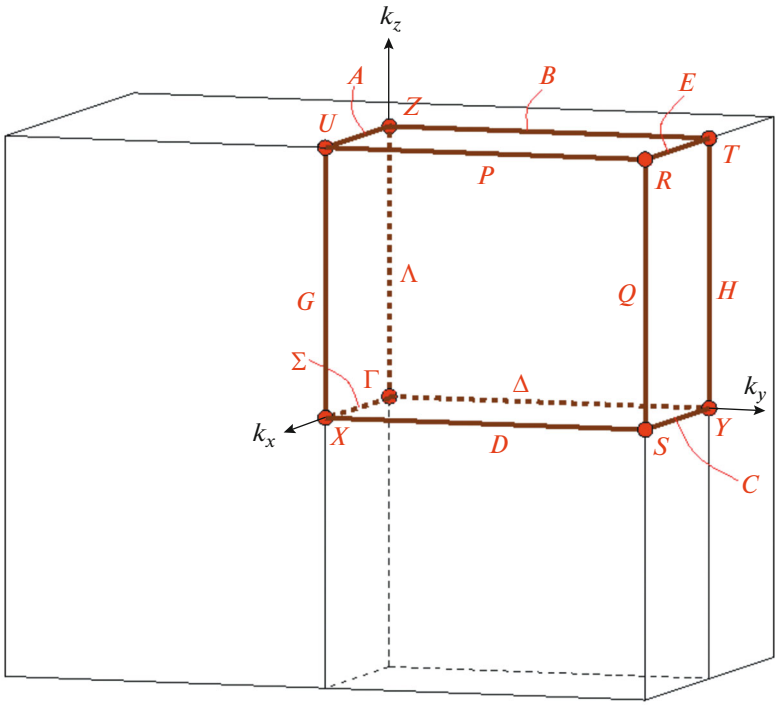

Fig. 2. Brillouin zone of the *Pnma* phase.

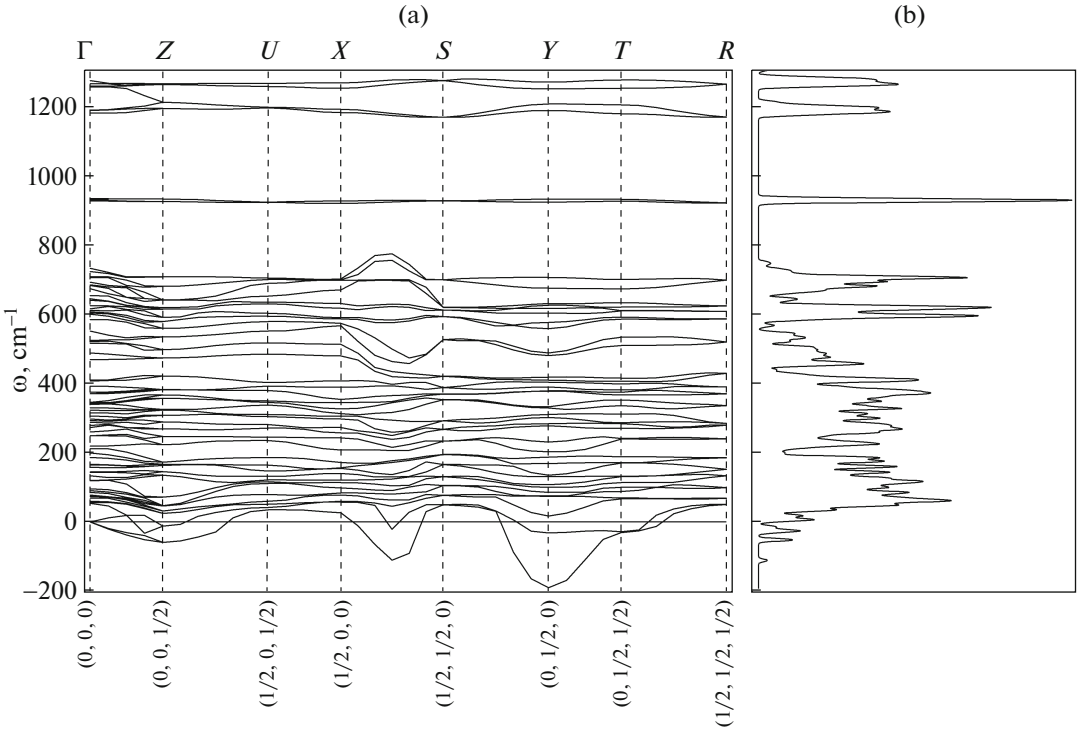

Fig. 3. (a) Dispersion and (b) phonon density of states for the $PbMnBO_4$ crystal in the *Pnma* phase.

The most unstable point between them corresponds to a frequency of 110.35*i* cm^{-1}. However, the most unstable and lowest-frequency mode in the entire phonon spectrum is at the point *Y* with a frequency of 189.47*i* cm^{-1}. The presence of unstable phonon modes indicates possible structural changes, as well as possible exis-

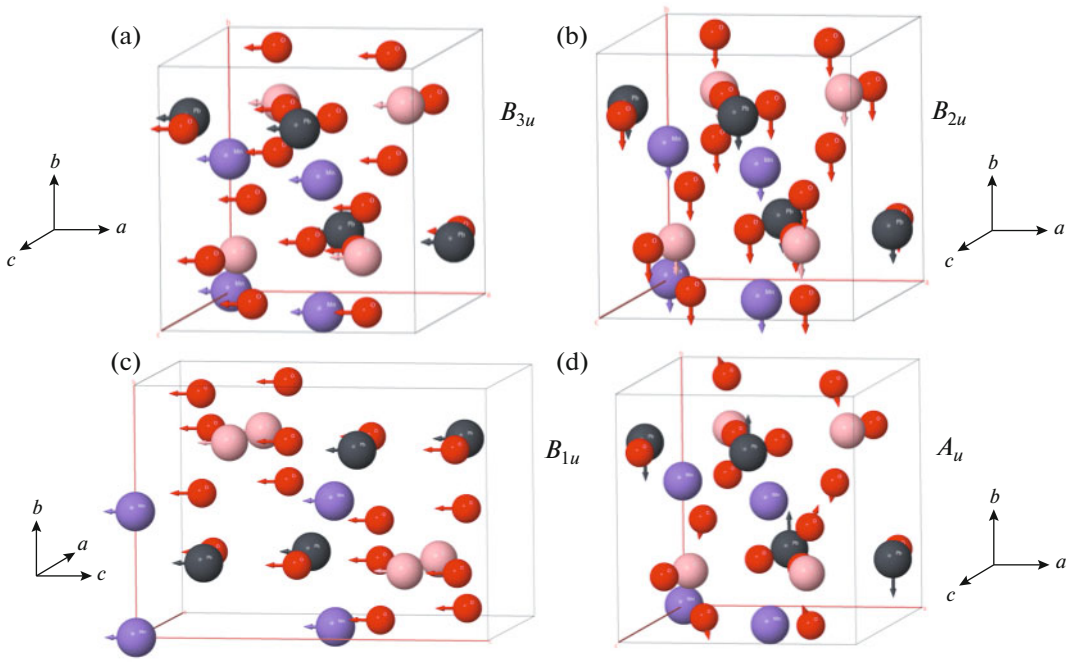

Fig. 4. Shape of low-frequency vibrations of the $PbMnBO_4$ crystal in the *Pnma* phase at the center of the Brillouin zone: (a) B_{3u}, (b) B_{2u}, (c) B_{1u}, and (d) A_u. According to the calculation, the frequencies of the vibrational modes with the B_{3u} and B_{2u} symmetries are very close to zero. The B_{1u} mode is also close to zero. The calculated frequency of the A_u mode is ~53.6 cm^{-1}.

tence of soft phonon modes in Raman spectra at a change in external parameters (temperature and pressure). Therefore, the soft temperature modes observed in the experimental vibrational spectra can be related not only to magnetic ordering but also to structural changes.

SELECTION RULES

To examine the vibrational spectrum at the center of the Brillouin zone in more detail, a symmetry analysis was performed. The unit cell of the crystal contains 28 atoms. The mechanical representation includes 84 modes. Among them, 3 are acoustic, 10 are inactive in the IR absorption and Raman processes, 36 are active in the Raman spectra, and 35 are active in the IR absorption processes. The selection rules are given in detail in Table 1. In particular, the data on the mechanical representation and active representations in the acoustic and optical ranges, as well as in the Raman and IR absorption processes at the center of the Brillouin zone, are listed.

According to this analysis, the calculated A_u mode with a frequency of 54 cm^{-1} is not observed in the Raman and IR absorption spectra. The manganese atom occupies the Wyckoff position 4*a* and, according to the selection rules, is not involved in the vibrational modes in the Raman spectrum.

The polarization selection rules are given in Table 2. They should be considered, since the experiment with different sample polarizations was previously performed [16]. This calculation will help to clarify some symmetry types and show the vibrations some modes correspond to. The designation V in Table 2 indicates the modes that can be observed in this scattering geometry. The first and sixth columns give the experimental configuration in the Porto notation [28].

RAMAN SPECTRUM

The theoretical Raman spectrum is shown in Fig. 5. It lies in the range from 50 to 1300 cm^{-1} and can be divided into four groups: high-frequency (from 1150 to 1300 cm^{-1}), then from 900 to 950 cm^{-1}, from 500 to 700 cm^{-1}, and from 50 to 450 cm^{-1}. Some low-intensity vibrations in the spectrum are not marked, but they are included in comparative Table 3. In this study, the shapes of all vibrations were determined; however, because of the article space limitations, only several most interesting modes are presented (Fig. 6).

The lowest frequency calculated vibration corresponds to the mode with parallel vibrations of boron and oxygen atoms in BO_2 triangles and displacements of oxygen atoms in MnO_6 octahedra and lead atoms (Fig. 6a). The next vibrational mode lies at 272 cm^{-1} and corresponds to the experimental mode at 224.7 cm^{-1} (Table 3). It was thoroughly studied in the experiment with a decrease in temperature and in an applied field [16]. The phonon A_g at 224.7 cm^{-1} demonstrated

Table 1. Atoms, Wyckoff positions, Raman tensor, and selection rules for the $PbMnBO_4$ crystal in the *Pnma* phase

Atom	Wyckoff position	Mechanical representation
Pb	4*c*	$2A_g + A_u + B_{1g} + 2B_{1u} + 2B_{2g} + B_{2u} + B_{3g} + 2B_{3u}$
Mn	4*a*	$3A_u + 3B_{1u} + 3B_{2u} + 3B_{3u}$
B	4*c*	$2A_g + A_u + B_{1g} + 2B_{1u} + 2B_{2g} + B_{2u} + B_{3g} + 2B_{3u}$
O	4*c*	$2A_g + A_u + B_{1g} + 2B_{1u} + 2B_{2g} + B_{2u} + B_{3g} + 2B_{3u}$
O	8*d*	$3A_g + 3A_u + 3B_{1g} + 3B_{1u} + 3B_{2g} + 3B_{2u} + 3B_{3g} + 3B_{3u}$
O	4*c*	$2A_g + A_u + B_{1g} + 2B_{1u} + 2B_{2g} + B_{2u} + B_{3g} + 2B_{3u}$

Raman tensor

A_g			B_{1g}			B_{2g}			B_{3g}		
a				*d*				*e*			
	b		*d*								*f*
		c				*e*				*f*	

Selection rules

$M = 11A_g + 10A_u + 7B_{1g} + 14B_{1u} + 11B_{2g} + 10B_{2u} + 7B_{3g} + 14B_{3u}$
$\Gamma_{acoust} = B_{1u} + B_{2u} + B_{3u}$
$\Gamma_{opt} = 11A_g + 10A_u + 7B_{1g} + 13B_{1u} + 11B_{2g} + 9B_{2u} + 7B_{3g} + 13B_{3u}$
$\Gamma_{IR} = 13B_{1u} + 9B_{2u} + 13B_{3u}$
$\Gamma_{Raman} = 11A_g + 7B_{1g} + 11B_{2g} + 7B_{3g}$

Table 2. Polarization selection rules for the $PbMnBO_4$ crystal in the *Pmna* phase (point group D_{2h})

	Backscattering geometry, 180°					Scattering geometry 90°, right angle			
	A_g	B_{1g}	B_{2g}	B_{3g}		A_g	B_{1g}	B_{2g}	B_{3g}
$-X(YY)X$	V				$X(YY)Z$	V			
$-X(YZ)X$				V	$X(YZ)Y$				V
$-X(ZZ)X$	V				$X(ZZ)Y$	V			
$-Y(XX)Y$	V				$Y(XX)Z$	V			
$-Y(XZ)Y$			V		$Y(XY)X$		V		
$-Y(ZZ)Y$	V				$Y(XY)Z$		V		
$-Z(XX)Z$	V				$Y(XZ)X$			V	
$-Z(XY)Z$		V			$Y(ZZ)X$	V			
$-Z(YY)Z$	V				$Z(XX)Y$	V			
					$Z(XY)X$		V		
					$Z(XZ)X$			V	
					$Z(XZ)Y$			V	
					$Z(YY)X$	V			
					$Z(YZ)X$				V
					$Z(YZ)Y$				V

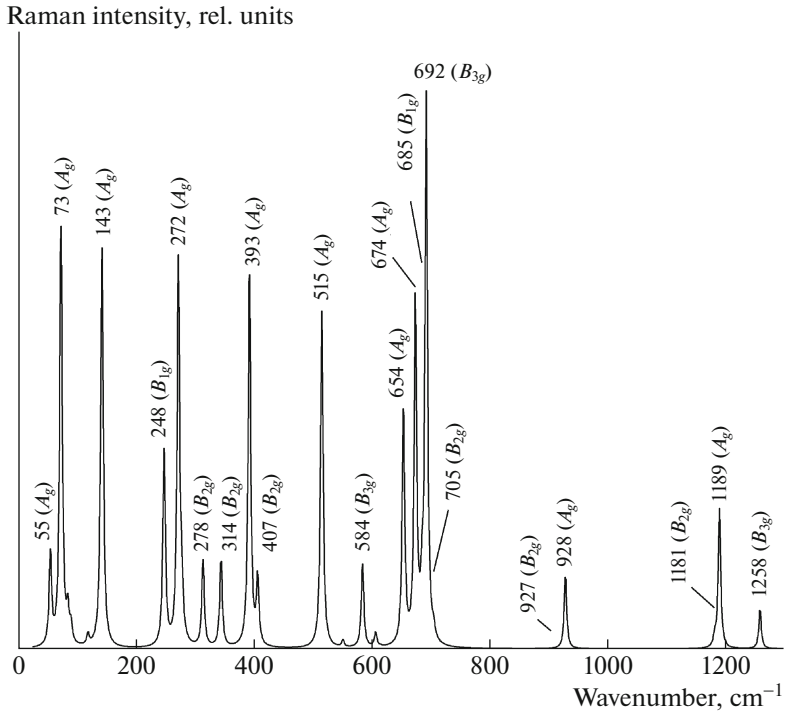

Fig. 5. Raman spectrum of the $PbMnBO_4$ crystal in the *Pnma* phase, obtained within the DFT in the plane-wave basis. The symmetry types and positions of the most intense modes are indicated.

a pronounced relationship between the lattice and magnetic subsystems in the experiment; this relationship manifested itself both in the frequency and in the renormalization of the Raman tensor below the critical temperature. A noticeable shift in the applied magnetic field was also revealed [16]. According to the calculation, the mode includes oxygen atom displacements, which distort MnO_6 octahedra (Fig. 6b). This confirms the assumption about possible interaction of the magnetic ordering and Jahn–Teller effect. The vibrational mode at 692.4 cm^{-1} is the most intense one in the calculated spectrum (Fig. 5); it corresponds to the experimental mode at 690.5 cm^{-1}. This mode includes vibrations of oxygen atoms in MnO_6 octahedra (Fig. 6c). The fully symmetrical vibration at 515 cm^{-1} corresponds to the experimental vibration at 526 cm^{-1} (Table 3). This mode contains a set of vibrations: scissor vibrations in BO_3 and vibrations of oxygen atoms in MnO_6 octahedra (Fig. 6d). The highest frequency mode at 1258 cm^{-1} corresponds to the experimental mode at 1294 cm^{-1}. It includes displacements of boron atoms and stretching vibrations of oxygen atoms in BO_3 triangles (Fig. 6e). The A_g vibrational mode at 1189 cm^{-1} corresponds to the experimental mode at 1224 cm^{-1}. This mode contains stretching vibrations: boron and oxygen atoms move towards each other (Fig. 6f).

Table 3 contains the Raman scattering data obtained by us, the experimental data from [16], and the calculation results from [18]. In [18], the calculation was carried out within the CRYSTAL09 program [29, 30] using the hybrid Hartree–Fock method and DFT [31]. This program uses atomic-orbital basis (the approximation in which the crystal orbital is a linear combination of atomic orbitals) rather than plane-wave bases. The program makes it possible to calculate the properties and electron wave functions of periodic systems.

The selection rules in this study and in the experimental study [16] are the same (Table 1). The calculated vibration frequencies in Table 3 are similar to the experimental ones, but the vibration types do not coincide. Unfortunately, the number of experimental B_{3g} and B_{2g} vibrations is inconsistent with the selection rules. The point is that the axes designations *a*, *b*, and *c* and the light backscattering geometry (180°) were chosen in the experiment [16]. Therefore, the *a* axis coincides with the tabular axis *y* and the *b* axis coincides with the *x* axis (Table 2). As a result, the B_{2g} and B_{3g} vibrational spectra are entangled. Unfortunately, in theoretical study [18], the number of B_{2g} and B_{3g} modes does not correspond to the selection rules either.

CONCLUSIONS

It was shown by the DFT calculation of the lattice dynamics at the high-symmetry points Γ–*Z*–*U*–*X*–*S*–*Y*–*T*–*R* that the *Pnma* phase of the $PbMnBO_4$ crys-

Table 3. Frequencies, symmetry types, and shapes of vibrations

This study (DFT), 0 K, plane waves			Experiment [7] 78 K		Calculation [10] (HF–DFT), 0 K, molecular orbitals		
frequency, cm^{-1}	symmetry type	vibration shape	frequency, cm^{-1}	symmetry type	frequency, cm^{-1}	symmetry type	vibration shape
55.4	A_g	O, B in BO_3, Pb displacements	49.4	A_g	52.1	A_g	Pb–O stretching
59.7	B_{3g}	Pb displacements O in BO_2, torsional	60.4	B_{3g}	63.6	B_{2g}	Pb–O–Pb rocking
73.2	A_g	O, B in BO_3, Pb displacements	64.6	B_{1g}	65.4	B_{1g}	O–Pb–O wobbling
74.5	B_{1g}	Pb, B parallel displacements O in BO_2 bending	90.8	B_{2g}	91.4	B_{3g}	Pb–O stretching
85.0	B_{2g}	Pb displacements	104.0	A_g	96.4	A_g	Pb–O stretching
90.5	B_{2g}	Pb displacements	108.6	B_{2g}	106.9	B_{3g}	Pb–O stretching
142.7	A_g	B, O in BO_3 parallel displacements	144.3	A_g	159.9	A_g	O–Pb–O scissor
119.1	B_{3g}	B, O in BO_3 displacements	185.6	B_{2g}	187.7	B_{2g}	Pb–O–Mn wobbling
144.4	B_{1g}	O in BO_2 torsional			189.5	B_{3g}	Pb–O stretching
198.8	B_{2g}	O in MnO_6 bending	186.7	B_{1g}	198.2	B_{1g}	O–Pb–O rocking
272.3	A_g	O in MnO_6 bending	224.7	A_g	213.9	A_g	Pb–O stretching
248.1	B_{1g}	O in BO_2 stretching asymmetric B, O displacements			226.8	B_{2g}	Pb–O–Mn wobbling
278.2	B_{2g}	BO bending	246.0	B_{2g}	251.4	B_{3g}	O–Mn–O torsional
287.8	B_{3g}	BO_3 bending	268.3	B_{1g}	273.3	B_{1g}	O–Mn–O wobbling
314.1	B_{2g}	O in MnO_2 stretching symmetric, BO stretching symmetric	283.9	A_g	283.2	A_g	Mn–O–Mn wobbling
340.9	B_{1g}	BO_3 bending	295.5	B_{3g}	294.7	B_{2g}	O–Mn–O torsional
344.0	B_{3g}	O–Mn–O torsional BO_3 bending	354.0	B_{2g}	360.0	A_g	Mn–O–Mn wobbling
344.8	A_g	MnO_6 bending, B displacements	355.0	B_{1g}	360.1	B_{3g}	Mn–O stretching
392.7	A_g	MnO_6 bending, BO_2 bending	363.8	A_g	363.8	B_{1g}	Mn–O stretching
406.7	B_{2g}		425.5	B_{2g}	426.7	B_{3g}	O–Mn–O torsional
515.4	A_g	BO stretching BO_2 scissor MnO_2 torsional	526.2	A_g	524.9	A_g	O–B–O torsional
551.2	B_{2g}	MnO_6 bending, BO_2 bending	531.2	B_{2g}	543.1	B_{3g}	Mn–O–Mn wobbling
584.4	B_{3g}	BO_3 bending	553.5	B_{3g}	561.6	B_{2g}	O–B–O scissor
606.6	B_{1g}	BO_3 bending	585.1	B_{1g}	599.3	B_{1g}	O–B–O scissor
615.5	B_{2g}	O–B–O scissor	613.7	B_{2g}	622.0	B_{3g}	O–B–O scissor
653.7	A_g	O–B–O scissor	624.8	A_g	633.0	A_g	O–B–O scissor
673.9	A_g	B displacements BO_3 bending	625.4	B_{1g}	633.6	B_{1g}	O–B–O scissor
685.1	B_{1g}	Parallel displacements O in Pb–O	667.7	B_{3g}	685.1	B_{2g}	O–B–O scissor
692.4	B_{3g}	O in MnO_6	690.5	A_g	694.4	A_g	O–B–O wobbling
705.1	B_{2g}	Parallel displacements O	728.8	B_{2g}	732.0	B_{3g}	O–B–O wobbling
927.4	B_{2g}	BO_3 stretching symmetric	915.2	B_{2g}	934.0	B_{3g}	B–O stretching, symmetric
928.2	A_g	O in BO_3 stretching, symmetric	927.1	A_g	947.4	A_g	B–O stretching, symmetric

Table 3. (Contd.)

This study (DFT), 0 K, plane waves			Experiment [7] 78 K		Calculation [10] (HF–DFT), 0 K, molecular orbitals		
frequency, cm^{-1}	symmetry type	vibration shape	frequency, cm^{-1}	symmetry type	frequency, cm^{-1}	symmetry type	vibration shape
1255.9	B_{1g}	O in BO_2 stretching, asymmetric, displacements B	1136.7	B_{1g}	1181.3	B_{1g}	B–O stretching, asymmetric
1181.1	B_{2g}	O, B in BO_3 stretching, symmetric	1138.7	B_{3g}	1183.3	B_{2g}	B–O stretching, asymmetric
1189.2	A_g	O, B in BO_3 stretching, symmetric	1224.0	A_g	1280.9	A_g	B–O stretching, asymmetric
1258.0	B_{3g}	O in BO_2 stretching, asymmetric, displacements B	1294.4	B_{2g}	1371.3	B_{3g}	B–O stretching, asymmetric

HF–DFT stands for the hybrid Hartree–Fock and DFT method.

tal is unstable at the points Γ, Z, and Y and in the D direction. Phonon branches occupy the region up to 1300 cm^{-1}. Three unstable phonon branches in the Z–Γ direction are acoustic, and one branch from point Z passes to the vibration with the A_u symmetry. The vibrations of such symmetry are inactive in the

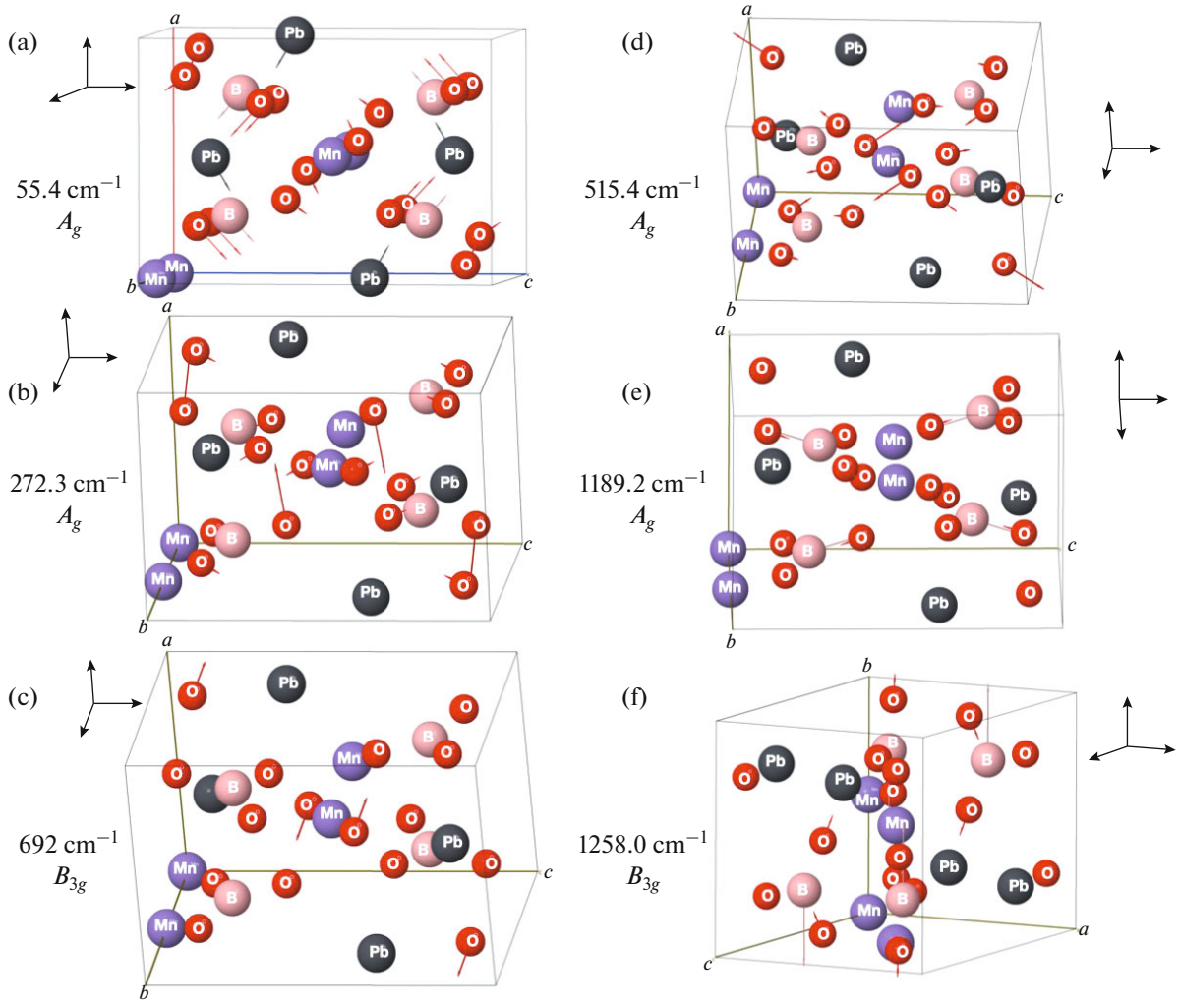

Fig. 6. Shapes of some vibrations in the Raman spectrum of the $PbMnBO_4$ crystal: (a) 55.4 cm^{-1} (A_g), (b) 272.3 cm^{-1} (A_g), (c) 692 cm^{-1} (B_{3g}), (d) 515.4 cm^{-1} (A_g), (e) 1189.2 cm^{-1} (A_g), and (f) 1258 cm^{-1} (B_{3g}).

Raman and IR absorption processes, according to the selection rules.

The DFT calculation of the Raman spectrum in the *Pnma* phase of the $PbMnBO_4$ crystal made it possible to obtain the frequencies of vibrations and determine their symmetry type and shapes. The results of the calculation are consistent with the results of previous experimental studies. A task of fundamental importance is to determine the shape of the vibration at 272.3 cm^{-1}, which corresponds to the experimental mode at 224.7 cm^{-1}. This mode corresponds to the bending vibrations of oxygen atoms in MnO_6 octahedra. This vibration shape confirms the assumption about possible relationship between the magnetic ordering and Jahn–Teller effect.

FUNDING

This study was supported by the Russian Foundation for Basic Research, project no. 21-52-12018 NNIO_a.

CONFLICT OF INTEREST

The author declares that she has no conflicts of interest.

REFERENCES

1. H. Park and J. Barbier, Acta Crystallogr. E **57**, i82 (2001). https://doi.org/10.1107/S1600536801013940
2. H. Park, J. Barbier, and R. P. Hammond, Solid State Sci. **5** (4), 565 (2003). https://doi.org/10.1016/S1293-2558(03)00056-6
3. H. Park, R. Lam, J. E. Greedan, and J. Barbier, Chem. Mater. **15**, 1703 (2003). https://doi.org/10.1021/cm0217452
4. W. Gao, Y. Jing, J. Yang, et al., Inorg Chem. **53**, 2364 (2014). https://doi.org/10.1021/ic403175w
5. K. Song, M. Yue, W. Gao, et al., J. Alloys Compd. **684**, 346 (2016). https://doi.org/10.1016/j.jallcom.2016.05.194
6. J. Yang and X. Sun, Int. J. Hydrogen En. **47** (61), 25608 (2022). https://doi.org/10.1016/j.ijhydene.2022.05.305
7. H.-J. Koo and M.-H. Whangbo, Solid State Commun. **149** (15–16), 602 (2009). https://doi.org/10.1016/j.ssc.2009.01.030
8. A. Pankrats, K. Sablina, D. Velikanov, et al., J. Magn. Magn. Mater. **353**, 23 (2014). https://doi.org/10.1016/j.jmmm.2013.10.018
9. M. M. Murshed, C. B. Mendive, M. Curti, et al., Mater. Res. Bull. **9**, 170 (2014). https://doi.org/10.1016/j.materresbull.2014.07.005
10. M. A. Prosnikov, A. N. Smirnov, V. Yu. Davydov, et al., J. Phys.: Condens. Matter **29**, 025808 (2017). https://doi.org/10.1088/0953-8984/29/2/025808
11. M. Curti, M. M. Murshed, T. Bredow, et al., J. Mater. Sci. **54**, 13579 (2019). https://doi.org/10.1007/s10853-019-03866-1
12. M. A. Prosnikov, Phys. Rev. B **103**, 094443 (2021). https://doi.org/10.1103/PhysRevB.103.094443
13. A. I. Pankrats, K. A. Sablina, D. A. Velikanov, et al., Solid State Phenom. **215**, 372 (2014). https://doi.org/10.4028/www.scientific.net/SSP.215.372
14. A. Pankrats, K. Sablina, M. Eremin, et al., J. Magn. Magn. Mater. **414**, 82 (2016). https://doi.org/10.1016/j.jmmm.2016.04.042
15. A. Pankrats, M. Kolkov, S. Martynov, et al., J. Magn. Magn. Mater. **471**, 416 (2019). https://doi.org/10.1016/j.jmmm.2018.09.098
16. M. A. Prosnikov, M. E. Bal, M. I. Kolkov, et al., Phys. Rev. Res. **4**, 013004 (2022). https://doi.org/10.1103/PhysRevResearch.4.013004
17. S. N. Martynov, Phys. Solid State **63**, 1253 (2021). https://doi.org/10.1134/S1063783421080199
18. Th. M. Gesing, C. B. Mendive, M. Curti, et al., Z. Kristallogr. **228** (10), 532 (2013). https://doi.org/10.1524/zkri.2013.1640
19. S. J. Clark, M. D. Segall, C. J. Pickard, et al., Z. Kristallogr. **220**, 567 (2005). https://doi.org/10.1524/zkri.220.5.567.65075
20. W. Kohn and L. J. Sham, Phys. Rev. **140**, A1133 (1965). https://doi.org/10.1103/PhysRev.140.A1133
21. P. C. Hohenberg, W. Kohn, and L. J. Sham, Adv. Quantum Chem. **21**, 7 (1990). https://doi.org/10.1016/S0065-3276(08)60589-4
22. B. G. Pfrommer, M. Côté, S. G. Louie, and M. L. Cohen, J. Comp. Physiol. **131**, 233 (1997). https://doi.org/10.1006/jcph.1996.5612
23. H. J. Monkhorst and J. D. Pack, Phys. Rev. B **13**, 5188 (1976). https://doi.org/10.1103/PhysRevB.13.5188
24. J. P. Perdew, K. Burke, and M. Ernzerhof, Phys. Rev. Lett. **77**, 3865 (1996). https://doi.org/10.1103/PhysRevLett.77.3865
25. J. P. Perdew, A. Ruzsinszky, G. I. Csonka, et al., Phys. Rev. Lett. **100**, 136406 (2008). https://doi.org/10.1103/PhysRevLett.100.136406
26. R. M. Hanson, *Enhancing Learning with Online Resources, Social Networking, and Digital Libraries,* Chap. Web-Based Molecular Visualization for Chemistry Education in the 21st Century, ACS Symposium Series (2010), p. 65. https://doi.org/10.1021/bk-2010-1060.ch004
27. J. G. Moberly, M. T. Bernards, and K. V. Waynant, J. Cheminform. **10**, 5 (2018). https://doi.org/10.1186/s13321-018-0259-x
28. D. L. Rousseau, R. P. Bauman, and S. P. S. Porto, J. Raman Spectrosc. **10**, 253 (1981). https://doi.org/10.1002/jrs.1250100152
29. R. Dovesi, R. Orlando, B. Civalleri, et al., Z. Kristallogr. **220**, 571 (2005).
30. R. Dovesi, V. R. Saunders, C. Roetti, et al., *CRYSTAL09 User's Manual* (Univ. of Torino, 2009).
31. T. Bredow and A. R. Gerson, Phys. Rev. B **61**, 5194 (2000). https://doi.org/10.1103/PhysRevB.61.5194

Translated by E. Bondareva